Article

Journal of the Brazilian Chemical Society

https://dx.doi.org/10.21577/0103-5053.20240140

J. Braz. Chem. Soc. **2024**, *35*, 12, e-20240140 , 1-13

Complex Oxides Synthesized via Arc Furnace: a Fast, Direct and Effective Approach to Obtain Functional Materials

Nadia G. Macedo,[a,b] *Miguel T. Galante,*[a,b] *Leonardo C. Soares,*[a,b] *Jéssica C. Alvim,*[a,b] *Vanderlei S. Lima,*[a,b] *Marcio Sangali,*[c] *João F. Q. Rodrigues,*[c] *Rubens Caram Jr.*[c] *and Claudia Longo*[*,a,b]

[a]*Instituto de Química, Universidade Estadual de Campinas (UNICAMP), 13083-970 Campinas-SP, Brazil*

[b]*Centro de Inovação em Novas Energias (CINE), Universidade Estadual de Campinas (UNICAMP), 13083-841 Campinas-SP, Brazil*

[c]*Faculdade de Engenharia Mecânica, Universidade Estadual de Campinas (UNICAMP), 13083-860 Campinas-SP, Brazil*

Complex oxides can present interesting semiconductor properties since the simultaneous presence of different metallic cations can modulate the conduction and valence band edges, affecting the bandgap energy, the onset potential for reactions and also the photocatalyst long-term stability. Here, we demonstrated that the synthesis of multinary oxides, very challenging using "traditional" methodologies, can be fast achieved by melting the precursor binary oxides in an arc furnace. As a proof of concept, arc-melting a mixture of Bi_2O_3 and V_2O_5 (Bi:V molar ratio of 1:1.05) resulted in almost pristine $BiVO_4$ (97.3% from Rietveld refinement of X-ray diffraction (XRD) data); photoelectrochemical (PEC) measurements indicated a promising application as a photoanode for O_2 evolution reaction. Conversely, the arc-melting of Bi_2O_3 and WO_3 mixture (Bi:W molar ratio of 2:1.15) resulted in the biphasic $Bi_2WO_6/Bi_2W_2O_9$; preliminary PEC analysis revealed characteristics of n-type semiconductor electrode with photoactivity under UV irradiation. Finally, the hierarchical Ag@α-$AgVO_3/Fe_2O_3$ consisted of micrometric Fe_2O_3 particles decorated by $AgVO_3$ nanoribbons and Ag nanoparticles, was obtained from melting Ag_2O, Fe_2O_3 and V_2O_5 as precursors (Ag:Fe:V molar ratio of 3:1:2); PEC measurements also revealed possible application as a photoanode. The results for these three materials demonstrated the arc-synthesis as a fast, effective and scalable methodology for synthesizing complex oxides.

Keywords: arc melting, synthesis, complex oxides, photoelectrochemical, PEC

Introduction

Complex oxides, which are oxides composed of two or more types of metallic cations, can be promising functional materials for application in several fields. These materials usually present a semiconductor character: after collecting solar radiation, the generation of electron-hole pairs can accelerate redox reactions of interest, such as photo-catalytical oxidation of organic contaminants in water, green hydrogen production from water splitting and CO_2 reduction to produce carbon-based fuels in a more sustainable way.[1,2]

In general, the most well investigated photoactive materials for such photoelectrochemical (PEC) applications are common binary oxides. Complex oxides can present improved properties compared to their binary counterparts and can offer promising opportunities in materials sciences and in PEC area. The simultaneous presence of different metallic cations can modulate the conduction and valence band (CB, VB) edges, affecting the bandgap energy (Eg), the onset potential for reactions and also the photocatalyst long-term stability.[3,4] Copper and silver oxides are elucidative examples: the binary oxides Cu_2O, CuO and Ag_2O would be interesting photoelectrodes considering their narrow Eg could provide excellent sunlight harvesting; however, these semiconductors present significant photocorrosion in

*e-mail: clalongo@unicamp.br
Editor handled this article: Célia M. Ronconi (Associate)
In honor to Prof. Oswaldo Luiz Alves, a worldwide recognized scientist, who provided inestimable contributions for the development of solid state chemistry and nanotechnology, and whose lectures were a source of inspiration and reflections about our role in science and society.

aqueous media. The introduction of a second metallic cation can tune the optoelectronic properties and the CB and VB edges, resulting in ternary copper (or silver) oxides with improved photostability in aqueous solution.[5,6]

Furthermore, the combination of the different transition metals results in thousands of possible compounds,[7] and very few are really known and well investigated, such as the case of $BiVO_4$, that is considered one of the most successful materials for the PEC oxygen evolution reaction (OER).[8]

Despite the promising features of ternary, or even quaternary (comprising three different cations) oxides, these materials can be very challenging to be synthesized via one single technique. Recently, our research group[9] reviewed the available methods to synthesize complex oxides. Generally, the resulting structures need very high temperatures for several hours to be formed (in some cases, near 1000 °C through traditional ceramic's solid-state reaction (SSR)). Furthermore, SSR usually results in relatively large grains, due to the agglomeration caused by the long periods of heating, and subsequent milling treatments are also required.[10] Wang *et al.*,[11] for instance, used a combination of milling and SSR reaction to obtain a vanadium doped $ZrSiO_4$. Although milling can be an effective way to decrease the size of particles, it must be carefully used to avoid drawbacks, like cross-contamination and even structural modifications.[9]

There are also several studies reporting the synthesis of complex oxides using well-known solution-based methods, like co-precipitation, hydrothermal, or sol-gel, which usually takes place at milder temperature conditions. Although these methods generally result in smaller particles compared to SSR, and in many cases, with well-defined morphology, the synthesis of complex oxides by these techniques usually require extra calcining steps, to improve crystallinity. As an example, Cai *et al.*[12] prepared by hydrothermal synthesis nanocomposites of $CuWO_4$/CuO (crystallite sizes of ca. 50 nm) for photodegradation of 4-nitrophenol. After the synthesis in autoclave (160-180 °C for 4 h), the sample was calcined at 600 °C for 3 h. Although faster than SSR + milling process, it is still a time-consuming synthesis procedure.

Moreover, these conventional methods generally result in the thermodynamically stable phases, which are not always the most active crystallographic structure of a material.[13] Alvarez-Roca *et al.*[14] obtained by co-precipitation Ag_2WO_4 polymorph, with three main crystallographic phases, the α-Ag_2WO_4 (orthorhombic), the β-Ag_2WO_4 (hexagonal), and the γ-Ag_2WO_4 (cubic), by varying the co-precipitation parameters, and using stabilizing agents. The β-Ag_2WO_4 showed the highest antimicrobial activity against methicillin-resistant *Staphylococcus aureus*, as well as the greatest performance for amiloride degradation under ultraviolet irradiation.[14]

Another challenge is the usual formation of secondary products or sub-stoichiometries.[3] However, this can occur in different synthesis methods, depending on the temperature, and reactants proportions. Thus, a phase diagram of the material, when available, can help to provide the best synthesis conditions.[15]

Compared to these currently used techniques, the use of the arc melting process can be a suitable alternative to the other methods since it permits the achievement of very high temperatures very quickly (seconds). For example, while traditional laboratory ovens can reach a maximum of approximately 1200 °C, in an arc furnace even temperatures as high as the vaporization of carbon (ca. 4500 K) can be attained.[16] Not surprisingly, breakthrough structures such as carbon nanotubes and fullerenes could arouse from the use of this technique.[17,18]

There are several types of melting systems, which can be divided in two larger cathegories: one using fuel as energy source (fuel-burning melting furnaces) and the other using electricity (electric melting furnaces). Electric melting systems can be subdivided in eletric-arc, plasma melting, and others. The basic principle of electric arc melting consists of an arc discharge caused, for example, by the short-circuiting of two electrodes like carbon, resulting in extreme high temperatures. In the case of the plasma melting, there is also the formation of a plasma formed from air or inert gas.[19] These conditions can be sufficient for melting metals and other precursors, sometimes producing rare structures, that are precluded in long-time reactions since they are not the most thermodynamically stable ones. Additionally, these short-time reactions not only prevent the agglomeration of grains problem that occurs in SSR, but also the necessity of further annealing steps to improve cristalinity generally required after solution-based techniques.

Arc melting method was scaled up by the metal melting industry and it has been used in several fields. For instance, an arc furnace is used in the first step to produce metallurgic grade Si from quartz crystals to be further treated and purified in different levels, either for the microelectronics or optoelectronics manufacture, among other industries.[20,21] Additionally, arc melting is also largely used to produce metal alloys.[22,23] For example, Caram and co-workers[24,25] have been studying the composition variation of Cu in high-entropy $CrCu_xFeMnNi$ and $CoCrCu_xFeNi$ alloys with semi-solid applications, among others, produced with arc melting technique, parting from practically pure elements' ingots. Moreover, arc melting synthesis can be

a facile and time-efficient method to tune the band gap of oxides materials.[26]

Despite the varied applications, and singular advantages, according to our knowledge, the use of an arc furnace to produce complex oxides is relatively new. Our research group, in collaboration with worldwide researchers, already reported[6,27] the synthesis of novel or rare complex oxides such as Cu_2WO_4 and $AgBiW_2O_8$, a ternary and a quaternary oxides with p-type semiconductor character, respectively. Both materials are being investigated as photocathodes in PEC reactors either for water decontamination, or for production of solar fuels from the CO_2 reduction reaction, CO_2RR.[1] Also, using arc-furnace, for the first time the crystallographic phase β-$AgBiW_2O_8$ was obtained with scheelite structure type with tetragonal space group I41/a and lattice parameters a = b = 5.3019 and c = 11.678 Å.[28] Before that, only a crystallographic phase with monoclinic symmetry and C2/m space group of the oxide was synthesized via solid-state, hydrothermal and solution combustion syntheses.[5,27,29]

In this work, we present the use of an arc furnace equipment to obtain three interesting materials based on complex oxides: practically pure monoclinic $BiVO_4$, multiphase $Bi_2WO_6/Bi_2W_2O_9$ and hierarchical Ag/α-$AgVO_3/Fe_2O_3$. The main structural and morphological characterizations were presented, and some preliminary PEC characterizations, and possible applications are discussed.

First, as a proof-of-concept of the arc synthesis, we discuss the preparation of $BiVO_4$, one of the most investigated n-type semiconductors for photocatalysis and photoelectrochemistry.[30] In this work, $BiVO_4$ was fast obtained by arc melting synthesis, and exhibited structural and photoelectrochemical properties comparable with those reported in literature for $BiVO_4$ obtained using different methodologies.

Bismuth tungstates have also been considered promising photocatalysts for several PEC systems. Bi_2WO_6 has an n-type conductivity, hence this ternary oxide can be applied as photoactive material to promote light-assisted oxidation reactions such as OER, alcohols oxidation reaction and pollutants degradation.[31-33] Furthermore, $Bi_2W_2O_9$, a well-known ferroelectric material, exhibits interesting properties for application as photocatalyst for OER and degradation of organic pollutants.[34] Compared to single bismuth or tungsten oxides, multiple metal species can be considered more favorable materials for ion storage, and charge transport, being pointed out as alternatives anodes to Li-ion battery.[35] Thus, we present the synthesis and properties of a multiphase material composed of different bismuth tungstates, $Bi_2WO_6/Bi_2W_2O_9$.

Finally, we discuss the arc synthesis and properties of a novel micro-nano composite, the Ag/α-$AgVO_3/Fe_2O_3$. Silver-based oxides, like silver vanadates, also present interesting optical properties, like band gap energies in the visible light range, but they are less studied for photoelectrochemical applications, in contrast with hematite, that is one of the most investigated photocatalysts and is an abundant and stable material.[5]

With this work we intend to present the versatility of arc melting technique in the synthesis of promising functional materials. This method is an alternative synthesis approach to produce well-stablished materials, or for lower investigated or novel structures among the plethora of possibilities from the combination of different metal oxides to generate more complex structures.

Experimental

Chemicals

All chemicals were used without further purification. Bi_2O_3, 99.9% purity, V_2O_5, 99.6% purity, WO_3, 99.9% purity, Fe_2O_3, 96%, powder < 5 μm, and Ag_2O, purity 99%, all from Sigma-Aldrich, Sant Louis, USA.

Arc furnace

The electric arc furnace (FCA Brasil, Campinas, Brazil) consisted of a stainless-steel chamber with a lateral glass window, copper, and tungsten electrodes, as represented in Figure 1.

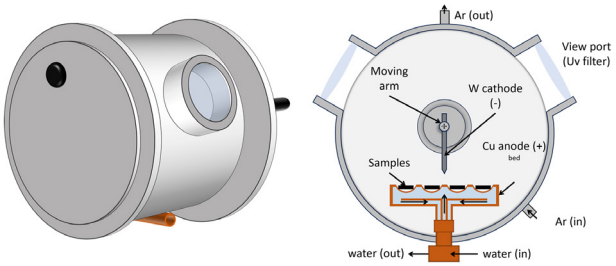

Figure 1. Scheme of arc furnace equipment.

General arc synthesis procedure

First, we prepared a mixture of pre-determined amounts of the binary oxides precursors, using an agate mortar; then, each mixture was compressed in a hydraulic press, resulting in pallets. The prepared pallets were placed, separately, on a water-cooled Cu hearth of an arc-melting furnace. The system was evacuated and then saturated with ultra-high pure argon (to form plasma), followed by

arc melting ignition (90 A) for approximately 30 s. The obtained products were further grinded using the agate mortar, resulting in powder samples that were washed several times, grinded and sieved.

$BiVO_4$

V_2O_5 and Bi_2O_3 were used as precursors, and 6 different vanadium to bismuth molar proportions were evaluated, including 1:1.05, 1:1.03, 1:1.01, 1:1, 1.03:1 and 1:05:1. Each mixture was homogenized, pressed in pallets, and melted in the arc furnace as previously described.

$Bi_2WO_6/Bi_2W_2O_9$

Bi_2O_3 and WO_3 were used as precursors, in a Bi:W molar ratio of 2:1.15.

Ag@α-$AgVO_3/Fe_2O_3$

Ag_2O, Fe_2O_3 and V_2O_5 were mixed up in a Ag:Fe:V molar ratio of 3:1:2.

Electrodes preparation

First, a suspension of particles (ink) of each complex oxide was prepared. $BiVO_4$ and $Bi_2WO_6/Bi_2W_2O_9$ inks were prepared by mixing the particles with polyethylene glycol (PEG) 20000 (Sigma-Aldrich, St. Louis, USA) and deionized water (mass proportion of 10:30:60). The Ag@α-$AgVO_3/Fe_2O_3$ ink was prepared by mixing 30 mg of particles with 185 μL of isopropanol (analytic grade, Synth, Diadema, Brazil) and 15 μL of Nafion™ (5% in alcoholic solution, Sigma-Aldrich, St. Louis, USA). Then, every suspension was magnetically stirred for 2 h. After that, thin films of each ink were deposited on the conductive substrate, glass with F-doped SnO_2 (FTO) (pieces with 1 × 3 cm). The FTO pieces were previously washed with Extran® (Sigma-Aldrich, St. Louis, USA), sonicated in a mixture of deionized water and ethanol (1:1) for 10 min, and then rinsed with deionized water. After delimiting the FTO surface with Kapton tape, 25 μL of the ink was dripped on 1 cm^{-2} of the FTO; after drying, the electrode was calcinated in muffle furnace (450 °C *per* 30 min, or 150 °C in one case for Ag@α-$AgVO_3/Fe_2O_3$ electrodes.

Morphological and structural analysis

The X-ray diffraction analyses (XRD) were performed in a XRD-7000 diffractometer (Shimadzu, Tokyo, Japan), with 40 kV and 30 mA, Cu Kα radiation (λ = 1.5406 Å). The Rietveld refinements were performed in Profex software[36] v 5.2.9 using the ICSD database. The UV-Vis-NIR (near infrared) spectra were recorded in reflectance mode in a spectrophotometer UV-2450 (Shimadzu, Tokyo, Japan) equipped with a sphere of integration. The morphology of the samples was examined with a Quanta FEG-250 field emission scanning electron microscope (FE-SEM, FEI Co., Hillsboro, USA), equipped with an Oxford X-MAX50 energy dispersive spectrometer (EDS) (Oxford, UK). Only for Ag@α-$AgVO_3/Fe_2O_3$ the microscopies were made on the LNNano Facility at CNPEM, in an equipment Thermo Fisher Scientific Helios Nano Lab 660 (Waltham, USA). The thermogravimetric (TGA) and differential calorimetric scanning (DCS) analysis were performed in a SDT Q-600 (TA Instruments, New Castle, USA).

(Photo)electrochemical measurements

All (photo)electrochemical measurements were performed at room temperature (24 °C), in a three-electrodes cell configuration. An Ag/AgCl (3 M KCl) (+0.197 V *vs*. reversible hydrogen electrode (RHE)) was used as reference electrode, and a Pt coil as counter-electrode. The (photo)currents were recorded under the illumination of a multimetallic vapor lamp (Osran Powers Star, 400 W). The cell was controlled by a potentiostat/galvanostat PGSTAT 128-N (Metrohm Autolab, Vantaa, Finland). The registered potentials were converted from the Ag/AgCl to the RHE scale by the following equation 1:

$$E_{RHE}\ (V) = E_{AglAgCl}\ (V) + 0.0591pH \quad (1)$$

Results and Discussion

Arc synthesis proof of concept: $BiVO_4$

Bismuth vanadate is a polymorph with a few known crystallographic structures, being the monoclinic scheelite (ms) the most relevant for water-splitting and biomass conversion.[37] This is due to its band gap (ca. 2.5 eV), with absorption of blue-violet light, low onset potential, and suitable band edge potentials for important oxidation reactions, for instance, OER. In this work, the ms-$BiVO_4$ particles were fast obtained by the arc-melting process.

Based on our previous experience, the main variable for the arc synthesis of $BiVO_4$ is the molar ratio between V_2O_5 and Bi_2O_3. Figure S1a (Supplementary Information (SI) section) displays the XRD of the as-synthesized oxides with different ratios of precursor. All samples mainly consisted of ms-$BiVO_4$ (ICSD No. 100603). The diffraction peaks 18.7°, 19.0°, 28.7°, 30.5°, 34.5°, 35.3°, 46.7°, 47.3°, 49.9°, 50.3° and 53.3° were associated to the (1 0 1), (0 1 1), (0 1 3), (0 4 0), (2 0 2), (0 2 0), (2 4 0), (2 –2 0), (2 2 0)

and (1 1 6) planes, respectively. However, a further analysis also reveals a secondary phase with Bragg angles 11.2°, 23.6°, 32.6°, 37.1°, 48.4° and 53.3°, which matches with the γ-Bi_2VO_5 pattern (ICSD No. 82271). Rietveld refinement of XRD data, performed for samples synthesized with V:Bi molar ratio corresponding to 1:1.05, 1:1 and 1.05:1 (Tables S1 and S2, SI section), revealed that these samples contained, respectively, 9.5, 3.8 and 2.7% of γ-Bi_2VO_5. Thus, the relative amount of Bi_2VO_5 in arc-synthesized $BiVO_4$ increased with the Bi quantity in the precursors. The sample synthesized with 5% excess of V_2O_5 consisted of 97.3% ms-$BiVO_4$ (Figure 2a), with refined lattice parameter a = 5.192 Å, b = 5.089 Å, c = 11.696 Å and β = 90.39°, in accordance with early reported results.[38] These results agree with the reported phase diagrams: various ternaries Bi-V oxides are expected to be formed in the bismuth-rich region, but only $BiVO_4$ is expected in the vanadium-rich region.[38-40]

Figure 2b shows the scanning electron microscopy of the sample synthesized with an excess of V_2O_5 (ca. 5%). For this analysis the resulting $BiVO_4$ pellet was manually ground in agata mortar, which resulted in particles with sizes varying from a few micrometers to sub-micron structures, with unidentified morphology. Here an important fact may have to be pointed out, the grain size may be impacted by the sample pulverization.

Figure 2c displays the thermogravimetric analysis of the as-synthesized powder, in oxidizing atmosphere. This measurement reveals the stability of the as-synthesized $BiVO_4$ at temperatures up to 600 °C. Additionally, the differential scanning calorimetry displays a small exothermic event at 200 °C, which was ascribed to the reintegration of oxygen from the atmosphere to the crystal. Probably, considering the absence of oxygen inside the arc-melting chamber, the fast melting could promote the oxygen vacancies on the resulting $BiVO_4$.[41]

The $BiVO_4$ UV-Vis absorption spectrum (Figure S1b, SI section), obtained through diffuse reflectance (DRS), displays a sharp absorption region of blue and ultraviolet light (λ ≤ 510 nm). Figure 2d shows the Tauc plot calculated from this measurement assuming a direct transition $(\alpha h\nu)^2$; then, the estimated band gap (Eg) corresponds to 2.45 eV, in excellent agreement with the literature.[42]

The potentiodynamic profile of the FTO|$BiVO_4$ (sample prepared with 5% excess of V_2O_5) was obtained in aqueous solution of 0.5 mol L^{-1} borate buffer (pH 9.2). The linear sweep voltammetry acquired under intermittent irradiation (Figure 2e) revealed that positive photocurrents were generated at potentials higher than the open-circuit potential (ca. +0.4 V *vs*. RHE), which is expected to occur in n-type semiconductors. The photocurrent densities display similar values to electrodes of $BiVO_4$ particles synthesized by the hydrothermal process.[34] Considering the Buttler-Gärtner approach,[35] from the variation of the square of photocurrent density as a function of applied potential (J^2 × Eapp) the flat band potential (EFB) was estimated at +0.42 V *vs*. RHE (Figure 2f).

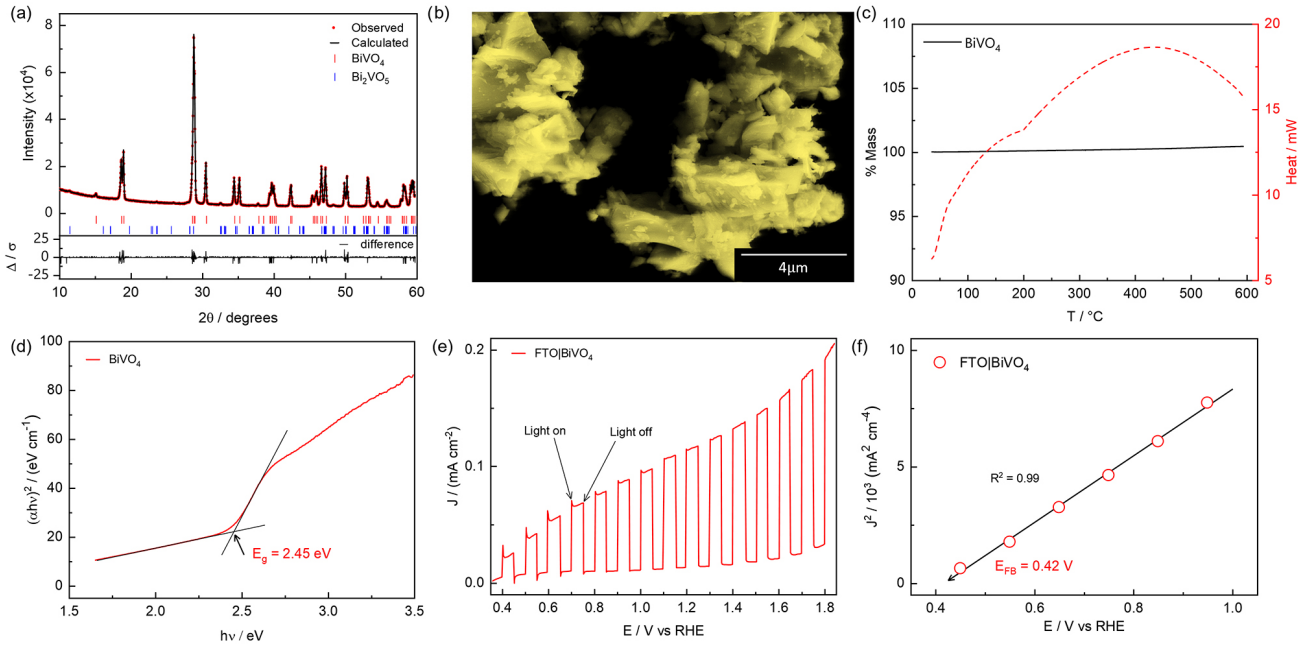

Figure 2. Characterization of the as-synthesized $BiVO_4$ powder (5% V_2O_5 excess). (a) X-ray diffraction, and Rietveld refinement; (b) scanning electron microscopy; (c) thermogravimetric analysis in oxidizing atmosphere; (d) Tauc plot for direct transition $(\alpha h\nu)^2 \times h\nu$. Photoelectrochemical properties of the FTO|$BiVO_4$ electrode in 0.5 mol L^{-1} borate buffer; (e) linear sweep voltammetry under intermittent irradiation; (f) Buttler-Gartner plot, J^2 × Eapp.

These results revealed that arc-synthesis can be considered a fast and simple method of generating pure $BiVO_4$ in the single monoclinic phase. Moreover, the particle size can be decreased by using high-energy pulverization methods and, since it is known that smaller particles present better catalytic and charge transport properties, the results obtained for the arc synthesized $BiVO_4$ can be improved.[37,43]

Arc synthesis of multiphasic materials: $Bi_2WO_6/Bi_2W_2O_9$

The n-type semiconductor Bi_2WO_6 can exist in orthorhombic structure at temperatures lower than < 960 °C, while at higher temperatures, the existing phase is monoclinic.[44] The Bi_2WO_6 presents orthorhombic Aurivillius perovskite structure, composed of $[Bi_2O_2]^{2+}$ and WO_6 octahedral layers, while $Bi_2W_2O_9$ is another representative of the Aurivillius phases with a layered arrangement of $[Bi_2O_2]^{2+}$ layers interleaved by $[W_2O_7]^{2-}$ sheets, as can be seen in (Figure 3).

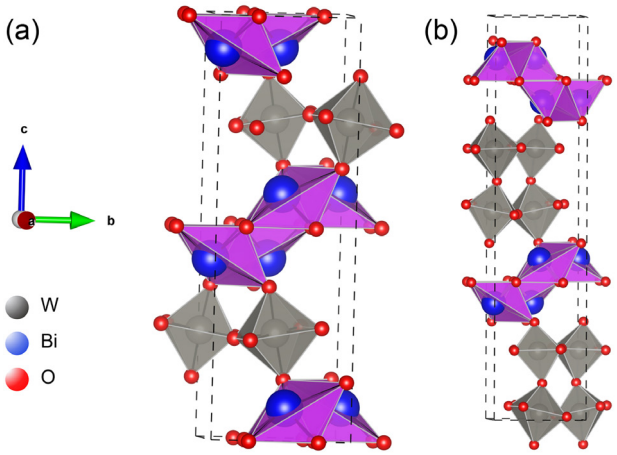

Figure 3. Schematic crystalline cell of (a) Bi_2WO_6 and (b) $Bi_2W_2O_9$ in the polyhedron mode.

Herein, we present the synthesis of $Bi_2WO_6/Bi_2W_2O_9$ samples synthesized through arc melting; to the best of our knowledge, it is the first time this multiphase material was synthesized by this methodology.

The XRD analysis of gray particles obtained through the arc melting method showed defined diffraction peaks, which could be assigned to $Bi_2W_2O_9$ and Bi_2WO_6, indicating the formation of a $Bi_2WO_6/Bi_2W_2O_9$ multiphasic material (Figure 4a). Heating the obtained material up to 600 °C did not change the mass of multiphasic sample (Figure S2, SI section), indicating that $Bi_2WO_6/Bi_2W_2O_9$ was thermically stable up to 600 °C. Tian *et al.*[45] did not observe obvious weight change in the TGA curve of $Bi_2W_2O_9$ single crystal sample in the temperature range between 50 and 950 °C. In the same way, Zhai *et al.*[46] did not distinguish a perceptible change in the weight of Bi_2WO_6 material in the TGA curve obtained from 100 to 800 °C.[46] Thus, it is not expected a phase transition for $Bi_2W_2O_9$ and Bi_2WO_6 between 100 and 800 °C. Moreover, the XRD analysis of $Bi_2WO_6/Bi_2W_2O_9$ electrode calcinated at 450 °C did not show diffraction peak related to a third crystalline phase (Figure S3, SI section). However, in the arc-melting method the complex oxide is synthesized in an inert atmosphere (Ar) and in a fast melting and solidification processes, we expect the generation of oxygen vacancies in the semiconductor structure prepared by this method. Therefore, the small increase (ca. 0.3%) in the weight of $Bi_2WO_6/Bi_2W_2O_9$ in temperatures above 250 °C and oxidative atmosphere can be associated with oxygen incorporation into the oxygen vacancies present in the $Bi_2WO_6/Bi_2W_2O_9$ lattice. DRS UV-Vis absorption spectrum of $Bi_2WO_6/Bi_2W_2O_9$ (Figure 4b) exhibited only a strong broad absorption band in the range from 330 to about 450 nm. Probably, the limited visible light absorption of sample based on Bi_2WO_6 and $Bi_2W_2O_9$ is caused by relatively large band gap of individual components which were estimated around 2.80 and 2.76 eV, respectively.[32,33,47]

SEM images (Figure 4c and inset) showed that $Bi_2WO_6/Bi_2W_2O_9$ sample is constituted of agglomerated particles with size range from submicrometer to 50 μm and ill-defined morphology. Chae *et al.*[31] grow nanostructures based on Bi_2WO_6 through two-step hydrothermal synthesis with subsequent thermal treatment, while Hill and Choi[48] reported a microporous film of Bi_2WO_6 obtained from a porous WO_3 electrode annealed with Bi^{3+} solution precursor on its surface. Regarding to $Bi_2W_2O_9$ there are few studies exploring the morphology of this material. Feteira and Sinclair[49] observed large-plate grains of $Bi_2W_2O_9$ obtained by SSR, otherwise, $Bi_2W_2O_9$ crystallites with plate-like shape were prepared by Mączka *et al.*[50] using Pechini method. Thus, it is important to note that different synthesis mechanisms can generate several structures based on Bi_2WO_6 and $Bi_2W_2O_9$ with distinct size and morphology that can be appropriate in accordance with the desired material application.

Figure S5b (SI section) shows cross-section image of $Bi_2WO_6/Bi_2W_2O_9$ film with the semiconductor particles adhered on the surface of FTO-glass substrate as well as the $Bi_2WO_6/Bi_2W_2O_9$ particles interconnected between them, indicating that FTO|$Bi_2WO_6/Bi_2W_2O_9$ photoelectrode has suitable electrical contact to allow the migration of charge carriers between the particles and their extraction through the external circuit. The (photo)electrochemical properties of FTO|$Bi_2WO_6/Bi_2W_2O_9$ were investigated in aqueous solution with 0.2 M Na_2SO_3 as hole acceptor

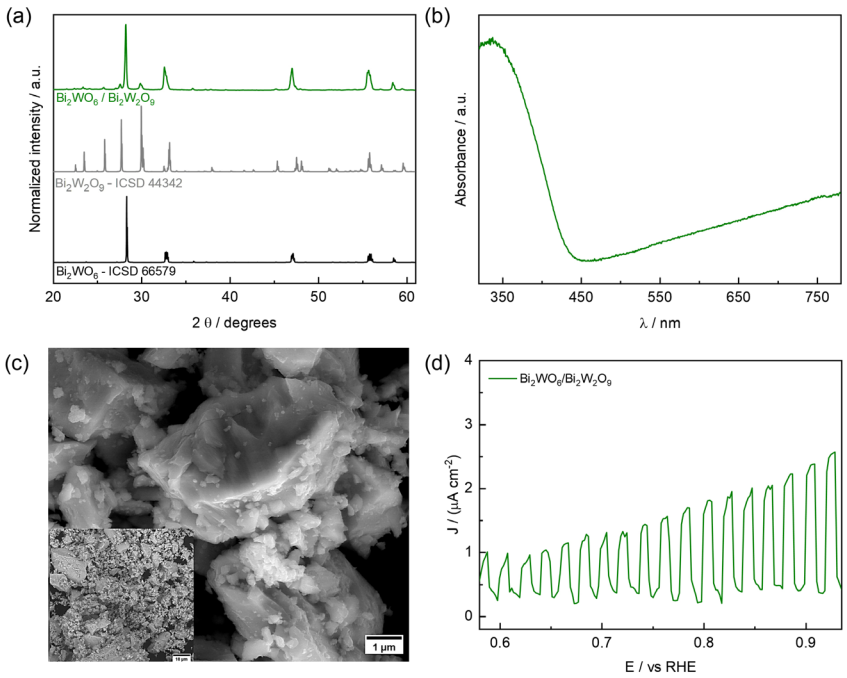

Figure 4. Characteristics of $Bi_2WO_6/Bi_2W_2O_9$ powder synthesized by arc-melting method. (a) XRD patterns; (b) UV-Vis absorption spectra; (c) SEM; (d) voltammogram obtained under intermittent irradiation for FTO|$Bi_2WO_6/Bi_2W_2O_9$ in aqueous 0.2 M Na_2SO_4 solution with 0.2 M Na_2SO_3 as hole acceptor.

specie. The linear sweep voltammetry under intermittent irradiation (Figure 4d) revealed a positive photocurrent which is an indicative of that electrode can be applied as a photoanode to promote oxidation reactions. However, the photocurrent is relatively low (ca. 3 µA cm^{-2}) in comparison to photoanodes prepared with semiconductors such as WO_3, $BiVO_4$ and Fe_2O_3.[51-53] As previously discussed, the wide band gap values of Bi_2WO_6 and $Bi_2W_2O_9$ can limit the photon absorption and, consequently, the generation of charge carriers in the FTO|$Bi_2WO_6/Bi_2W_2O_9$.

Furthermore, Moss *et al.*[54] studied the origin of low photocurrent generated by Bi_2WO_6 photoanode using transient absorption spectroscopy (TAS) and highlighted that electron extraction in this material is at least 10 times slower than the slowest kinetics previously reported for TiO_2, $BiVO_4$ and WO_3 photoanodes. As a result of the wide band gap of Bi_2WO_6 and $Bi_2W_2O_9$ and low charge carrier transportation, a low photocurrent was expected for sample in comparison to other semiconductors such as $BiVO_4$ and Fe_2O_3. These intrinsic limitations of Bi_2WO_6 for photoelectrochemical application can be also observed in other synthesis method chosen for the material preparation. For example, Bera *et al.*[55] showed that Bi_2WO_6 sample synthesized by hydrothermal method generate ca. 6 µA cm^{-2} for OER at 1.23 V *vs.* RHE. Concomitantly, Zhang *et al.*[56] demonstrated that Bi_2WO_6 semiconductor prepared by template-directed synthesis generated 5 and 20 µA cm^{-2} at 1.0 V *vs.* RHE for OER with a nonporous and porous films, respectively.

To overcome this challenge, several strategies have been applied to improve the photoactivity of Bi_2WO_6 and $Bi_2W_2O_9$ such as heterojunction with different semiconductors to improve the charge carrier extraction,[48] cocatalyst modification,[57] and doping.[58,59] In addition, since Zhang *et al.*[60] showed that n-n junction between n-type semiconductor $Bi_2W_2O_9$ and n-type semiconductor WO_3 increased the response of the $WO_3/Bi_2W_2O_9$ as H_2S gas sensor, this could also be an application for $Bi_2WO_6/Bi_2W_2O_9$ material. Therefore, Bi_2WO_6 and $Bi_2W_2O_9$ exhibited interesting properties that can be improved for application as photocatalyst in PEC systems.

Arc synthesis of multiphasic materials: hierarchical Ag@α-$AgVO_3/Fe_2O_3$

$AgVO_3$ is a polymorph with different known crystallographic phases, namely α-$AgVO_3$, β-$AgVO_3$, δ-$AgVO_3$, and γ-$AgVO_3$. The best known are the monoclinic phases β-$AgVO_3$ (space group C2/c) which is thermodynamically stable, and the metastable α-$AgVO_3$ (Cm). This last one is generally obtained in room temperature, or by quenching the melt of $AgVO_3$.[61-63]

In this work we describe a novel material synthesized via arc synthesis, from a mixture of Ag, Fe, and V binary oxides in a 3:1:2 molar proportion, respectively. The diffractogram patterns exhibited in Figure 5a presents peaks of α-Fe_2O_3 (hematite), α-$AgVO_3$, and metallic Ag, as can be seen from the comparison of the experimentally obtained

sample and the respective ICSD patterns. Figure 5b exhibits the absorbance profile, derived from UV-Vis DRS data, where it is possible to observe a stronger absorption from UV light in the blue region of visible-light spectrum, and with a similar profile to other α-Fe_2O_3 composites found in literature,[64,65] like Fe_2O_3/g-C_3N_4, showing a possible predominance of Fe_2O_3 optical properties. This is expected since the absorption profile is generally governed by the lowest band gap material. While α-Fe_2O_3 presents an Eg of ca. 2.0-2.2 eV,[9] experimental values for α-$AgVO_3$ are in the order of 2.4-2.7 eV.[62,66]

The obtaining of the α-$AgVO_3$ metastable crystallographic structure in the high temperatures of arc melting instead of the thermodynamically stable β-$AgVO_3$ is interesting, since the first is usually obtained at low temperatures. However, this kind of result is not uncommon, since these high temperatures are reached very quickly. However, after synthesized, α-$AgVO_3$ is known to be irreversibly converted to the β-$AgVO_3$ in temperatures above 200 °C. The thermogravimetric and differential thermal analyses of the sample are depicted on Figure S4a (SI section), showing an event starting a little before 400 °C. According to Kittaka *et al.*,[63] a large exothermic peak appears at 381 °C, followed by an endothermic peak (474 °C), from DTA analysis in air of a mixture of Ag_2O-V_2O_5 precursors. The first peak is assigned to the formation of β-$AgVO_3$ and the second with its melting point. They also mentioned that the crystal enthalpy decreases in the order α-$AgVO_3$, δ-$AgVO_3$, and β-$AgVO_3$, being the β-$AgVO_3$ the most stable phase.[63]

SEM combined to EDS microanalysis (Figure 5) provide important information about the morphology, and the local composition of the sample. Figures 5c-5e bring SEM micrographs of the composites in different magnifications. Figures 5c and 5d are secondary electrons (SE) detector images, that evidence the topographic details of the sample. In the first image it is possible to see clusters with micrometric size covered with needle-like nanostructures. In the higher magnification image in Figure 5d, it is more evident that the structures are nanoribbons-like, which can be better visualized in the Figure S4b (SI section). Figure 5e brings an image made with backscattered (BS) electrons detector, where the contrast is associated to compositional details. It is possible to observe the presence of brighter nanoparticles on some regions of the ribbons. This higher brightness is associated with higher atomic

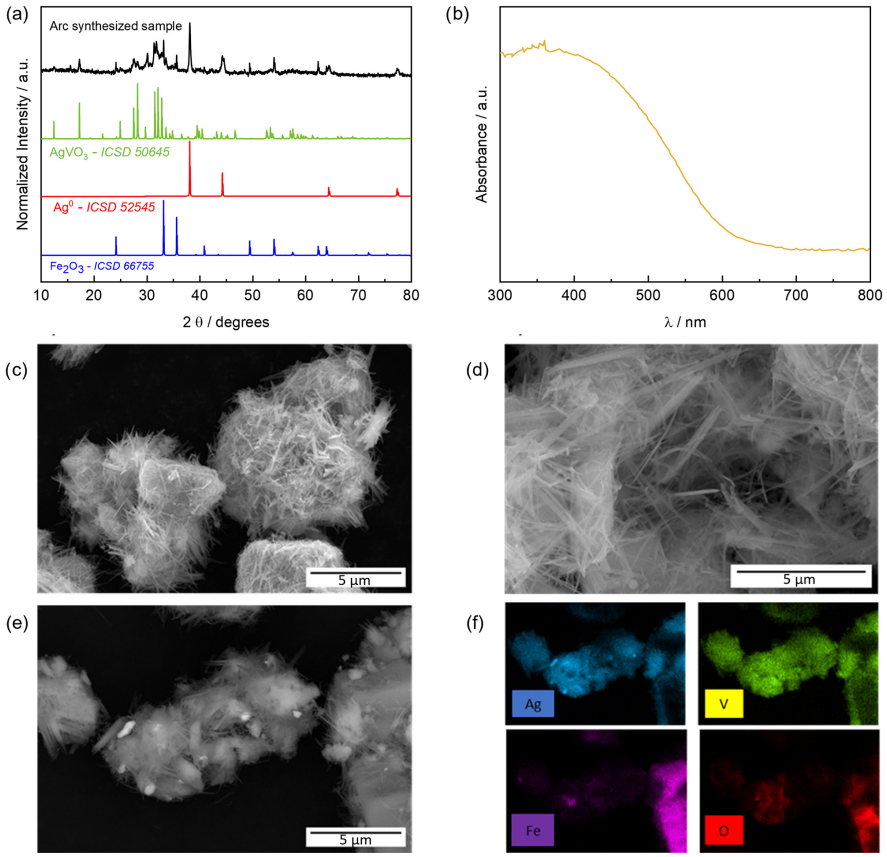

Figure 5. (a) Normalized XRD patterns of powder sample synthesized via arc melting technique and ICSD patterns of component materials; (b) absorption spectrum from UV-Vis DRS data for Ag/α-$AgVO_3$/Fe_2O_3 arc melting obtained powder sample; (c-e) FE-SEM images of the synthesized powder composite; (f) EDS compositional mapping of selected region of image.

number elements; thus, the particles are probably formed by silver. To confirm the composition distribution, EDS compositional analysis mapping was performed for the same region in Figure 5f, which points out that iron is more distributed along the micro grains, while vanadium and silver appears along the nanoribbons. Silver also appears strongly on the brighter nanoparticles observed for the BS images, confirming the composition of NPs. In this sense, the collected images indicate that micrometric grains of hematite are decorated with silver vanadate nanoribbons, that are also covered with Ag nanoparticles on the surface, forming an interesting hierarchical material. Literature[63,66] reports frequently show the morphology of α-$AgVO_3$ as fine needle-like (or ribbons/rods) crystallites. Hierarchical materials, i.e., organized with a multi-length scale, can be very interesting for different technological applications. Nature itself, for instance, builds up hierarchical biological structures like bones, a composite of hydroxyapatite and proteins organized into a multilength-scale structural hierarchy.[67]

Additionally, the presence of metallic Ag nanoparticles (NPs) can provide quantum effects due to the diminutive size, presenting peculiar properties such as localized surface plasmon resonance effect (LSPR). The LSPR phenomenon involves the collective oscillation of conduction band electrons of plasmonic nanostructures, established when the illumination frequency is resonant with the natural oscillation frequency of metals free electrons.[68] This can be an important addition to applications that require visible light illumination, helping, e.g., to broaden the spectral absorption range, enhance the local electromagnetic field and generate thermal effect.[69]

Photoelectrodes of the hierarchical composite were prepared by depositing an alcoholic dispersion of Ag/α-$AgVO_3$/Fe_2O_3 particles on FTO. Generally, the electrodes preparation involves the addition of PEG in the dispersion and a thermal treatment near 450 °C for PEG elimination. Since this thermal treatment could not be used with α-$AgVO_3$, an alcoholic suspension of the semiconductor particles was directly deposited on FTO followed by heat treatment up to 150 °C, resulting in a dark-green electrode. Figure S5c (SI section) is a cross sectional image of the as-prepared electrode, showing good film adhesion (also visually observed during experiments). For comparison, the electrodes were also prepared by doctor blade coating, followed by heating at 450 °C (which causes the phase transition from α to β-$AgVO_3$); then, orange electrodes were obtained, but also with good visual adhesion.

Then, it was performed some PEC measurements with both electrodes in a neutral electrolyte (0.2 M Na_2SO_4 aqueous solution), in N_2 saturated medium and with 0.2 M Na_2SO_3 as hole scavenger. Figure 6a displays the potentiometries zero current to registry the open circuit potential (OCP) variation in dark and after polychromatic irradiation. Both the electrodes show a potential decay after illumination, which is a typical behavior of n-type semiconductor electrodes, and the electrode heated at 450 °C shows a significative value. Linear voltammetries registered under intermittent irradiation revealed that only the electrode heated at 450 °C (β phase) presented a positive photocurrent density, circa of 10 μA cm^{-2}. Considering that silver vanadates usually behave as p-type semiconductor electrodes, the PEC properties of FTO|Ag/$AgVO_3$/Fe_2O_3 thus revealed the prevalence of hematite (n-type semiconductor).

In addition, the cyclic voltammetries also show a higher dark current for the electrode containing β-$AgVO_3$. The increase on the capacitive current can be associated with morphology changes or even the enlargement of porosity on the electrode surface. As mentioned, the thermal treatment altered the electrodes color from dark green (heating at 150 °C) to orange (heating at 450 °C) (see Figure S4c, SI section). The absorbance spectra for both the electrodes were presented in Figure 6d.

The color of the electrodes also changed, going from dark green (electrode heated at 150 °C) to orange (electrode heated at 450 °C) (see Figure S4c). These changes can also be pointed out on the absorbance spectrum, which is broader in the case of the second one, with some variations in the band positions and a tail in the infrared region.

In accordance with literature reports,[70] the β-$AgVO_3$ exhibits improved optical properties and better performance for PEC applications. Also, a non-aqueous electrolyte could be more convenient, however, we preferred the aqueous media considering a greener strategy. A p-n junction of $AgVO_3$/Mo-$BiVO_4$ was constructed by Gao *et al.*[71] for PEC water oxidation reaction. The $AgVO_3$/Mo-$BiVO_4$ photoanodes boosted the photocurrent density by 7 folds at 1.23 V *vs*. RHE and moved the onset potential negatively by 387 mV compared to the bare $BiVO_4$. The composites were prepared via a simple successive ionic layer adsorption and reaction. The nanostructures of $AgVO_3$ (3-5 nm) were grown on the molybdenum dopped $BiVO_4$ surface.[71]

To the best of our knowledge, the only report of a successful direct use of the α-$AgVO_3$ phase of silver vanadate for photoelectrochemical PEC application was reported by Chowdhury *et al.*[66] First, they synthesized α-$AgVO_3$ nanorods (NRs) via co-precipitation method at relatively low temperature (35 °C); then α-Fe_2O_3-NPs@ $AgVO_3$-NRs were prepared trough wet-impregnation method followed by solvent evaporation, with α-Fe_2O_3

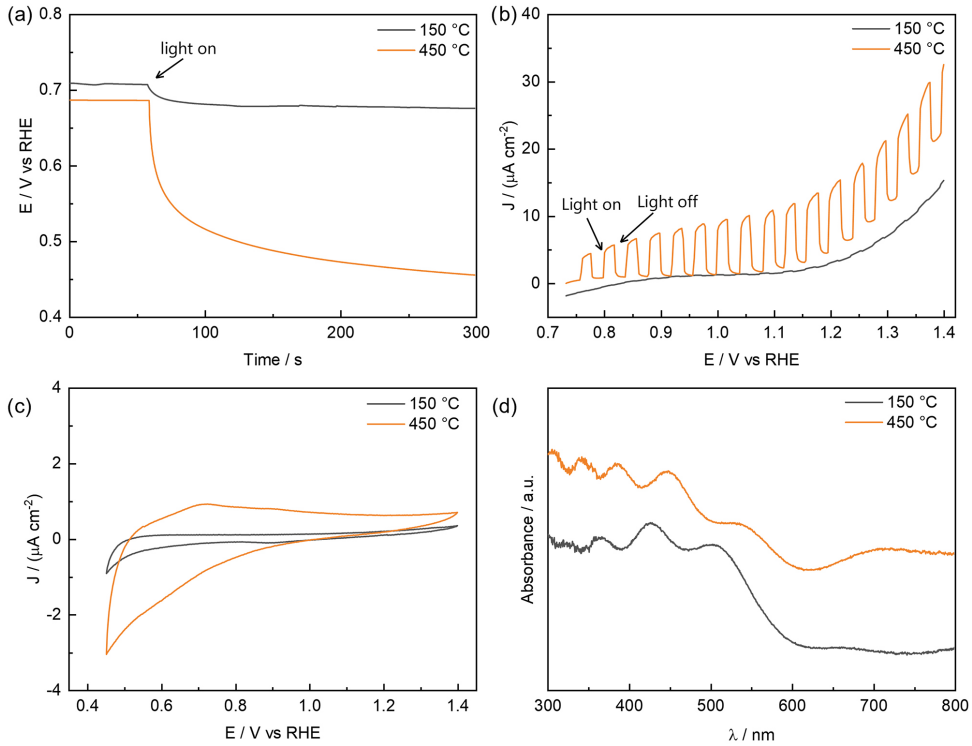

Figure 6. Characterization of electrodes prepared with arc-synthesized $Ag/AgVO_3/Fe_2O_3$ with a post thermal treatment at 150 or 450 °C, in 0.2 M Na_2SO_4 solution with 0.2 M Na_2SO_3 as hole acceptor. (a) Potentiometry zero current; (b) photovoltammogram under intermittent irradiation (20 mV s^{-1}); (c) cyclic voltammetries (in dark) (20 mV s^{-1}); (d) UV-Vis DRS absorption spectra for both electrodes.

previously prepared via hydrothermal method. The semiconductors were combined in a final Z-scheme heterojunction, with porous structure and the electrode was used for OER. The photoanode exhibited OER overpotential of 1.05 mV *vs*. RHE and photocurrent density of around 6.2 mA cm^{-2} in 0.5 M KOH under standard illuminations conditions AM 1.5 G.[66] Authors did not mention a possible phase change during preparation step and they attributed the high performances to the high surface area and abundant active sites. The exposed Fe_2O_3 nanoparticles on the surface of silver vanadate is also a possible explanation.

It is also worth discussing the presence of Ag NP on the arc-synthesized $Ag/AgVO_3/Fe_2O_3$. Ag NPs, as well as Ag^+ ions, act as effective antimicrobial agents; also, Ag oxides generally act as efficient photocatalysts for organic pollutants degradation. As an example, α-$AgVO_3$/hydroxyapatite composites with photocatalytic and anti-fungal properties were synthesized through co-precipitation method by da Silva *et al.*[72] The composites, in different proportions, showed improved results compared to the isolated counterparts on dye discoloration; the 22.5 wt.% HA/α-$AgVO_3$ resulted in 85% of discoloration after 60 min under UV illumination. The composites could also inhibit the growth of *Fusarium* and *Colletotrichum* species, *in vitro*.[72] Thus, considering the interesting properties of $Ag/AgVO_3/Fe_2O_3$ components, this arc-synthesized material can be evaluated as photocatalyst for decontamination and disinfection of water.

Conclusions

In this work we presented three types of materials recently obtained by our research group using an arc furnace facility. The first was the well-known m-$BiVO_4$, traditionally used as photocatalyst in the OER and other applications. The synthesized $BiVO_4$ shows similar photoelectrochemical properties of the same material synthesized via widely employed hydrothermal synthesis, for example, and the performance can be improved by efficient comminution methods. The second material was a n-n junction based on two different bismuth tungstates, the $Bi_2WO_6/Bi_2W_2O_9$, that can also be applied as photocatalyst absorbing UV light. Finally, a novel composite of Ag NPs, the metastable α-$AgVO_3$ and the traditional binary oxide Fe_2O_3. This last is a multiscale material, here named as hierarchical, since it is composed of micrometric particles of Fe_2O_3 decorated by α-$AgVO_3$ nanoribbons, which are covered with Ag NPs. More than focus on the materials applications, the aim of this work was to present the arc melting methodology as a fast, direct, and scalable technique on the production of several promising complex structures and metastable materials.

Supplementary Information

Supplementary information consists of five separate figures, and two tables, composed by additional characterization and is available free of charge at http://jbcs.sbq.org.br as PDF file.

Acknowledgments

The authors gratefully acknowledge support from CNPq (processes 131552/2020-1, 306948/2021-4, 150861/2022-2), Coordination of Superior Level Staff Improvement (CAPES) finance code 001, FAPESP (São Paulo Research Foundation, process 2017/11986-5, 2018/18293-8, 2021/05853-8, 2019/08270-3), Shell and the strategic importance of the support given by ANP (Brazil's National Oil, Natural Gas and Biofuels Agency) through the R&D levy regulation. This research used facilities of the Brazilian Nanotechnology National Laboratory (LNNano), part of the Brazilian Centre for Research in Energy and Materials (CNPEM), a private non-profit organization under the supervision of the Brazilian Ministry for Science, Technology, and Innovations (MCTI). The electron microscopy staff is acknowledged for the assistance during the experiments (2021104477). The authors also thank to Professor Italo Odone Mazali and Lucas Magno Freitas Oliveira for thermal analysis.

Author Contributions

Nadia G. Macedo, Miguel T. Galante, Leonardo. C. Soares and Jéssica C. Alvim equally contributed to this paper, being responsible for the synthesis of materials, main characterization, paper elaboration, writing and editing. Vanderlei S. Lima, Márcio Sangali, and João Rodrigues performed some synthesis, characterization, and participated into the discussions of results. Rubens Caram authorized the use of arc melting equipment and participated of some discussions and suggestions. Claudia Longo supervised the research, administered the project and revised and wrote the article.

References

1. de Medeiros, J. F.; Galante, M. T.; Bertazzoli, R.; dos Santos, C. G. P.; Longo, C.; *ACS ES&T Water* **2022**, *2*, 982. [Crossref]
2. Sun, S.; Wang, W.; *RSC Adv*. **2014**, *4*, 47136. [Crossref]
3. Sivula, K.; van de Krol, R.; *Nat. Rev. Mater.* **2016**, *1*, 15010. [Crossref]
4. Roger, I.; Shipman, M. A.; Symes, M. D.; *Nat. Rev. Chem.* **2017**, *1*, 0003. [Crossref]
5. Galante, M. T.; Sotelo, P.; Hossain, M. K.; Vali, A.; Raamann, A.; Longo, C.; Macaluso, R. T.; Rajeshwar, K.; *ChemElectroChem* **2019**, *6*, 87. [Crossref]
6. Galante, M. T.; Živković, A.; Alvim, J. C.; Kleiner, C. C. C.; Sangali, M.; Taylor, S. F. R.; Greer, A. J.; Hardacre, C.; Rajeshwar, K.; Caram, R.; Bertazzoli, R.; Macaluso, R. T.; de Leeuw, N. H.; Longo, C.; *ACS Appl. Mater. Interfaces* **2021**, *13*, 32865. [Crossref]
7. Kim, J. S.; Kim, B.; Kim, H.; Kang, K.; *Adv. Energy Mater.* **2018**, *8*, 1702774. [Crossref]
8. Tan, H. L.; Amal, R.; Ng, Y. H.; *J. Mater. Chem. A* **2017**, *5*, 16498. [Crossref]
9. Macedo, N. G.; Alvim, J. C.; Soares, L. C.; da Costa, L. S.; Galante, M. T.; Lima, V.; Longo, C.; *Mater. Adv.* **2024**, *5*, 4541. [Crossref]
10. Merkle, R.; Maier, J.; *Angew. Chem., Int. Ed*. **2008**, *47*, 3874. [Crossref]
11. Wang, T.; Liu, J.; Jiang, W.; Jiang, F.; Feng, G.; Miao, L.; Zhang, Q.; Wu, Q.; Lao, X.; *Ceram. Int.* **2022**, *48*, 24044. [Crossref]
12. Cai, Y.; Yang, F.; Wu, L.; Shu, Y.; Qu, G.; Fakhri, A.; Gupta, V. K.; *Mater. Chem. Phys.* **2021**, *258*, 123919. [Crossref]
13. Gouveia, A. F.; Roca, R. A.; Macedo, N. G.; Cavalcante, L. S.; Longo, E.; San-Miguel, M. A.; Altomare, A.; da Silva, G. S.; Andrés, J.; *J. Mater. Res. Technol.* **2022**, *21*, 4023. [Crossref]
14. Alvarez-Roca, R.; Gouveia, A. F.; de Foggi, C. C.; Lemos, P. S.; Gracia, L.; da Silva, L. F.; Vergani, C. E.; San-Miguel, M.; Longo, E.; Andrés, J.; *Inorg. Chem.* **2021**, *60*, 1062. [Crossref]
15. Schorne-Pinto, J.; Cassayre, L.; Presmanes, L.; Barnabé, A.; *Inorg. Chem.* **2019**, *58*, 6431. [Crossref]
16. Atkins, P.; *Shriver and Atkins' Inorganic Chemistry*; Oxford University Press: Oxford, 2010.
17. Iijima, S.; *Nature* **1991**, *354*, 56. [Crossref]
18. Krätschmer, W.; Lamb, L. D.; Fostiropoulos, K.; Huffman, D. R.; *Nature* **1990**, *347*, 354. [Crossref]
19. Sakai, S.; Hiraoka, M. In *Waste Materials in Construction - Putting Theory into Practice*, vol. 71; Goumans, J. J. J. M.; Senden, G. J.; van der Sloot, H. A., eds.; Elsevier: Netherlands, 1997.
20. Eriksson, G.; Hack, K.; *Woodhead Publishing Series in Metals and Surface Engineering*, 2nd ed.; Woodhead Publishing, Cambridge, UK, 2008.
21. Knight, R.; Smith, R. W.; Apelian, D.; *Int. Mater. Rev.* **1991**, *36*, 221. [Crossref]
22. Terentyev, D.; Khvan, T.; You, J.-H.; Van Steenberge, N.; *J. Nucl. Mater.* **2020**, *536*, 152204. [Crossref]
23. da Costa, F. H.; Pinhão, R.; dos Anjos, S.; Caram, R.; Fogagnolo, J. B.; *Mater. Lett.* **2020**, *260*, 126901. [Crossref]
24. Campo, K. N.; de Freitas, C. C.; da Fonseca, E. B.; Caram, R.; *Mater. Charact*. **2021**, *178*, 111260. [Crossref]
25. Campo, K. N.; de Freitas, C. C.; Fanton, L.; Caram, R.; *J. Mater. Sci. Technol*. **2020**, *52*, 207. [Crossref]
26. Ou, G.; Li, D.; Pan, W.; Zhang, Q.; Xu, B.; Gu, L.; Nan, C.; Wu, H.; *Adv. Mater.* **2015**, *27*, 2589. [Crossref]

27. Longo, C.; Galante, M. T.; Fitzmorris, R.; Zhang, J. Z.; Taylor, S. F. R.; Mohapatra, J.; Liu, J. P.; Duarte, L. G. T. A.; Hossain, M. K.; Hardacre, C.; Rajeshwar, K.; *J. Phys. Chem. C* **2018**, *122*, 13473. [Crossref]
28. Sotelo, P.; Moore, M.; Galante, M. T.; Longo, C.; Rajeshwar, K.; Suescun, L.; Macaluso, R. T.; *Polyhedron* **2019**, *170*, 486. [Crossref]
29. de Tacconi, N. R.; Timmaji, H. K.; Chanmanee, W.; Huda, M. N.; Sarker, P.; Janáky, C.; Rajeshwar, K.; *ChemPhysChem* **2012**, *13*, 2945. [Crossref]
30. Kamble, G. S.; Natarajan, T. S.; Patil, S. S.; Thomas, M.; Chougale, R. K.; Sanadi, P. D.; Siddharth, U. S.; Ling, Y.-C.; *Nanomaterials* **2023**, *13*, 1528. [Crossref]
31. Chae, S. Y.; Lee, E. S.; Jung, H.; Hwang, Y. J.; Joo, O.-S.; *RSC Adv.* **2014**, *4*, 24032. [Crossref]
32. Wang, F.; Zhou, X.; Li, J.; He, Q.; Zheng, L.; Liu, Q.; Chen, Y.; Zhang, G.; Liu, X.; Li, H.; *Molecules* **2021**, *26*, 7334. [Crossref]
33. Nascimento, L. L.; Marinho, J. Z.; dos Santos, A. L. R.; de Faria, A. M.; Souza, R. A. C.; Wang, C.; Patrocinio, A. O. T.; *Appl. Catal. A* **2022**, *646*, 118867. [Crossref]
34. Alfaro, S. O.; Martínez-de la Cruz, A.; *Appl. Catal. A* **2010**, *383*, 128. [Crossref]
35. Liang, Y.; Shi, J.; Fang, B.; *Chem. Phys. Lett.* **2019**, *716*, 112. [Crossref]
36. Döbelin, N.; *Profex*, version 5.2.9; Switzerland, 2024; Döbelin, N.; Kleeberg, R.; *J. Appl. Crystallogr.* **2015**, *48*, 1573.
37. Shi, H.; Guo, H.; Wang, S.; Zhang, G.; Hu, Y.; Jiang, W.; Liu, G.; *Energy Fuels* **2022**, *36*, 11404. [Crossref]
38. Swanson, H. E.; Morris, M. C.; Evans, E. H.; Ulmer, L.; *Standard X-Ray Diffraction Powder Patterns*; United States, Government Printing Office: Washington, D.C., 1964. [Link] accessed in July 2024
39. Touboul, M.; Vachon, C.; *Thermochim. Acta* **1988**, *133*, 61. [Crossref]
40. Lv, P.; Zheng, M.; Wang, X.; Huang, F.; *J. Alloys Compd.* **2014**, *583*, 285. [Crossref]
41. Jiamprasertboon, A.; Sertwatsana, S.; Ngamwongwan, L.; Sangkhun, W.; Waehayee, A.; Phonsuksawang, P.; Bootchanont, A.; Nijpanich, S.; Busayaporn, W.; Nakajima, H.; Suthirakun, S.; Butburee, T.; Siritanon, T.; *New J. Chem.* **2023**, *47*, 14758. [Crossref]
42. Mascaro, L. H.; Pockett, A.; Mitchels, J. M.; Peter, L. M.; Cameron, P. J.; Celorrio, V.; Fermin, D. J.; Sagu, J. S.; Wijayantha, K. G. U.; Kociok-Köhn, G.; Marken, F.; *J. Solid State Electrochem.* **2015**, *19*, 31. [Crossref]
43. Yabuta, M.; Takeda, A.; Sugimoto, T.; Watanabe, K.; Kudo, A.; Matsumoto, Y.; *J. Phys. Chem. C* **2017**, *121*, 22060. [Crossref]
44. Yoneda, Y.; Kohara, S.; Takeda, H.; Tsurumi, T.; *Jpn. J. Appl. Phys.* **2012**, *51*, 09LE06. [Crossref]
45. Tian, X.; Gao, Z.; Chen, F.; Wu, Q.; Li, C.; Lu, W.; Sun, Y.; Tao, X.; *CrystEngComm* **2018**, *20*, 2669. [Crossref]
46. Zhai, J.; Yu, H.; Li, H.; Sun, L.; Zhang, K.; Yang, H.; *Appl. Surf. Sci.* **2015**, *344*, 101. [Crossref]
47. Kang, D.; Park, Y.; Hill, J. C.; Choi, K.-S.; *J. Phys. Chem. Lett.* **2014**, *5*, 2994. [Crossref]
48. Hill, J. C.; Choi, K.-S.; *J. Mater. Chem. A* **2013**, *1*, 5006. [Crossref]
49. Feteira, A.; Sinclair, D. C.; *J. Am. Ceram. Soc.* **2008**, *91*, 1338. [Crossref]
50. Mączka, M.; Ptak, M.; Kępiński, L.; Tomaszewski, P. E.; Hanuza, J.; *Vib. Spectrosc.* **2010**, *53*, 199. [Crossref]
51. Francàs, L.; Selim, S.; Corby, S.; Lee, D.; Mesa, C. A.; Pastor, E.; Choi, K.-S.; Durrant, J. R.; *Chem. Sci.* **2021**, *12*, 7442. [Crossref]
52. Yang, T.-Y.; Kang, H.-Y.; Sim, U.; Lee, Y.-J.; Lee, J.-H.; Koo, B.; Nam, K. T.; Joo, Y.-C.; *Phys. Chem. Chem. Phys.* **2013**, *15*, 2117. [Crossref]
53. Corby, S.; Francàs, L.; Kafizas, A.; Durrant, J. R.; *Chem. Sci.* **2020**, *11*, 2907. [Crossref]
54. Moss, B.; Le, H.; Corby, S.; Morita, K.; Selim, S.; Sotelo-Vazquez, C.; Chen, Y.; Borthwick, A.; Wilson, A.; Blackman, C.; Durrant, J. R.; Walsh, A.; Kafizas, A.; *J. Phys. Chem. C* **2020**, *124*, 18859. [Crossref]
55. Bera, S.; Samajdar, S.; Pal, S.; Das, P. S.; Jones, L. A. H.; Finch, H.; Dhanak, V. R.; Ghosh, S.; *Ceram. Int.* **2022**, *48*, 35814. [Crossref]
56. Zhang, L.-W.; Wang, Y.-J.; Cheng, H.-Y.; Yao, W.-Q.; Zhu, Y.-F.; *Adv. Mater.* **2009**, *21*, 1286. [Crossref]
57. Yu, H.; Liu, R.; Wang, X.; Wang, P.; Yu, J.; *Appl. Catal. B* **2012**, *111-112*, 326. [Crossref]
58. Zhang, L.; Man, Y.; Zhu, Y.; *ACS Catal.* **2011**, *1*, 841. [Crossref]
59. Yang, X.; Ma, Y.; Liu, Y.; Wang, K.; Wang, Y.; Liu, M.; Qiu, X.; Li, W.; Li, J.; *ACS Appl. Mater. Interfaces* **2021**, *13*, 19864. [Crossref]
60. Zhang, Y.; Zhang, X.; Guo, C.; Xu, Y.; Cheng, X.; Zhang, F.; Major, Z.; Huo, L.; *ACS Appl. Mater. Interfaces* **2020**, *12*, 54946. [Crossref]
61. Kittaka, S.; Matsuno, K.; Akashi, H.; *J. Solid State Chem.* **1999**, *142*, 360. [Crossref]
62. da Silva, J. S.; Machado, T. R.; Martins, T. A.; Assis, M.; Foggi, C. C.; Macedo, N. G.; Beltrán-Mir, H.; Cordoncillo, E.; Andrés, J.; Longo, E.; *Inorg. Chem.* **2019**, *58*, 5900. [Crossref]
63. Kittaka, S.; Nishida, S.; Iwashita, T.; Ohtani, T.; *J. Solid State Chem.* **2002**, *164*, 144. [Crossref]
64. Guo, H.; Chen, M.; Zhong, Q.; Wang, Y.; Ma, W.; Ding, J.; *J. CO2 Util.* **2019**, *33*, 233. [Crossref]
65. Liang, Y.-C.; Hsu, Y.-W.; *Int. J. Mol. Sci.* **2021**, *22*, 6884. [Crossref]
66. Chowdhury, A.; Balu, S.; Yang, T. C.-K.; *J. Environ. Chem. Eng*. **2023**, *11*, 109769. [Crossref]
67. Yao, L.; Wang, Y.; Zhao, J.; Zhu, Y.; Cao, M.; *Small* **2023**, *19*, 2208101. [Crossref]

68. Wang, S.-S.; Hu, W.-C.; Liu, F.-F.; Xu, Q.-Y.; Wang, C.; *Electrochim. Acta* **2019**, *301*, 359. [Crossref]
69. Lv, S.; Du, Y.; Wu, F.; Cai, Y.; Zhou, T.; *Nanoscale Adv.* **2022**, *4*, 2608. [Crossref]
70. Vali, A.; Sarker, H. P.; Jee, H. W.; Kormányos, A.; Firouzan, F.; Myung, N.; Paeng, K.-J.; Huda, M. N.; Janáky, C.; Rajeshwar, K.; *ChemPhysChem* **2019**, *20*, 2635. [Crossref]
71. Gao, L.; Long, X.; Wei, S.; Wang, C.; Wang, T.; Li, F.; Hu, Y.; Ma, J.; Jin, J.; *Chem. Eng. J.* **2019**, *378*, 122193. [Crossref]
72. da Silva, J. S.; Machado, T. R.; Trench, A. B.; Silva, A. D.; Teodoro, V.; Vieira, P. C.; Martins, T. A.; Longo, E.; *Mater. Chem. Phys.* **2020**, *252*, 123294. [Crossref]

Submitted: February 10, 2024
Published online: July 25, 2024